

<https://doi.org/10.1038/s41612-025-01092-y>

Decadal variability of summer extreme heat in central-eastern China and its synergistic effects by the North Atlantic and tropical western Pacific SST

Tiejun Xie¹, Hui Gao²✉, Ting Ding²✉, Xintong Chen³ & Wei Wang⁴

It was found that the Central-eastern China's summer extreme heat (CECSH) has a decadal variability with a cycle of about 70 years and is significantly positively correlated with the Atlantic Multidecadal Oscillation (AMO) core area sea surface temperature (SST; AMO_{CORE}) and the tropical western Pacific SST (WPSST) in boreal summer. Diagnostic analyses such as synergistic diagnostic and linear baroclinic model (LBM) experiments show that the warm AMO_{CORE} and WPSST in boreal summer can generate the localized heat dome (HD) over Mongolia to northeast China by exciting local convection and subsequent propagation, respectively, which in turn directly influences the CECSH decadal variability through compression of the atmosphere and temperature transport. The empirical models of the CECSH decadal variability were constructed based on the AMO_{CORE} or the WPSST separately and synergistically considering both, and the empirical model considering the synergistic effects of the AMO_{CORE} and the WPSST had better simulation capability.

In recent years, extreme weather and climate events have become more frequent around the world, and extreme heat has also increased in frequency and intensity under the background of global warming^{1–9}. For example, many areas of the world experienced record-breaking heat events in 2022. On July 16–19, 2022, England experienced an unprecedented extreme heat event, with Coningsby reaching 40.3 °C on the 19th, breaking the English air temperature record by 1.5 °C and also marking the first time the air temperature in England exceeded 40 °C^{10,11}. In the late spring and early summer of 2022, many areas of South Asia, including India and Pakistan, experienced a prolonged period of extreme heat, with air temperatures consistently exceeding the climatological mean state by up to 8 °C in some months, leading to severe human casualties, agricultural production losses, and glacial lake outbursts¹². Furthermore, severe summer extreme heat events have occurred in many parts of Europe, the Mediterranean, and North America^{10,13–15}. Summer extreme heat has occurred more frequently in the global region in recent years, which was also highlighted in the IPCC AR6 Synthesis Report¹⁶.

In recent years, summer extreme heat in China has also become more frequent and intense, and the Central-eastern China (CEC) region

(20°–40°N, 90°–120°E) has become the fastest developing center of summer extreme heat in the Asian monsoon region¹⁷. In the summer of 2022, many areas of the CEC experienced the strongest extreme heat event from 1961 to that time, and the immediately following summer of 2023 again surpassed the summer of 2022 to set a new historical record^{16,9,17–20}. In addition, the CEC region has also experienced higher frequency or intensity of summer extreme heat events in 2018, 2019, 2020, 2021, and other recent years^{21–24}. Stronger summer extreme heat for 6 consecutive years from 2018 to 2023 at least means that the occurrence of the CEC's summer extreme heat (CECSH) is not just a contribution from annual variability, but there may also be significant decadal variability that can persist over a longer period, accompanied by the external forcing effects of anthropogenic warming. CEC is one of the world's major population centers with a high risk of exposure to extreme heat^{25–27}, and high frequency or intensity of summer extreme heats can have important impacts on regional ecology, agricultural production, health and energy deployment^{28–32}, especially if the summer heat extremes persist for more than a decade. Thus, it is of great scientific importance and societal value to study the decadal variability of the CECSH and to identify its underlying mechanisms.

¹Beijing Municipal Climate Center, Beijing Meteorological Bureau, Beijing, 100089, China. ²State Key Laboratory of Climate System Prediction and Risk Management/China Meteorological Administration Climate Studies Key Laboratory, National Climate Center, China Meteorological Administration, Beijing, 100081, China. ³Anhui Province Key Laboratory of Atmospheric Science and Satellite Remote Sensing, Anhui Institute of Meteorological Sciences, Hefei, 230031, China. ⁴Pinggu District Meteorological Bureau, Beijing Meteorological Bureau, Beijing, 101200, China. ✉e-mail: gaohui@cma.gov.cn; dingting@cma.gov.cn

There are more studies on the annual variability of the CECSH or individual case analyses, but fewer studies on its long-term decadal variability^{21,33–37}. For example, Chen and Lu³⁴ analyzed the local circulation differences corresponding to summer extreme heat in different regions of eastern China, but it remains unclear how these local circulations are modulated by other climate factors. Wang et al.³⁷ found that the summer North Atlantic Oscillation (NAO) and the northwest Pacific sea surface temperature (SST) have synergistic effects on the extreme heat events in the CEC on an interannual timescale, but the relationship on decadal timescales has not been studied. Ding and Ke³⁵ investigated the spatial and temporal characteristics of heat wave events in China between 1960 and 2013, and pointed out that the decadal variability of heat wave events in China is remarkable, but the reasons for this remain unexplained. Also, the decadal here is limited to the last 50 or 60 years and may be more of a trend than a true long period of decadal shift, e.g., China³⁸ and America³⁹ in the 1930s or Prague-Klementinum⁴⁰ and Ukraine⁴¹ in the 1940s were also peak periods of extreme heat. Compared to the recent extreme heat, the extreme heat of the 1930s and 1940s was clearly influenced by less human activity, suggesting that the CECSH may have a decadal variability. Xie et al.⁴² analyzed the decadal variability of annual temperature in the CEC and its mechanism, but the decadal variability of summer extreme heat in the CEC has not yet been investigated.

The external forcing signals on summer extreme heat, especially the extreme heat trends of recent years, emphasized the effect of human activities or the greenhouse effect^{1,12,15}, but how can the extreme heat of the

1930s be explained? For external oceanic forcings, such as El Niño-Southern Oscillation (ENSO), the tropical Indian Ocean, and the Atlantic Ocean, the focus has also been limited to extreme heat in recent years, with more annual or near-decadal trends^{21,37}, again failing to show why the summer extreme heat of the 1930s was another concentration period. Thus, it is essential to study the long-series decadal variability of the CECSH. Here, the decadal variability of the CECSH and its mechanism are analyzed on the basis of a long time series of daily maximum temperature data from 1900 to 2019, and it is found that the decadal variability of the CECSH undergoes a synergistic effect of the Atlantic Multidecadal Oscillation (AMO; also known as the AMV^{13,44}) core area SST (AMO_{CORE}) and the tropical western Pacific SST (WPSST). The synergistic mechanism of the AMO_{CORE} and the WPSST on the decadal CECSH is revealed, and an empirical model for the decadal CECSH with good predictive performance is constructed. It should be noted that the study period of this paper ends in 2019 due to data availability and also to avoid the impact of the super-anomalous extreme heat of the last two years on this study.

Results

Decadal variability of the CECSH and its relation to the AMO_{CORE} and the WPSST

Firstly, the measured daily maximum temperatures from the Xujiahui meteorological observatory in Shanghai, covering a long period from 1873 to the present, were used to test the reliability of the Berkeley Earth daily maximum temperatures in the CEC. As shown in Fig. 1a, the summer-

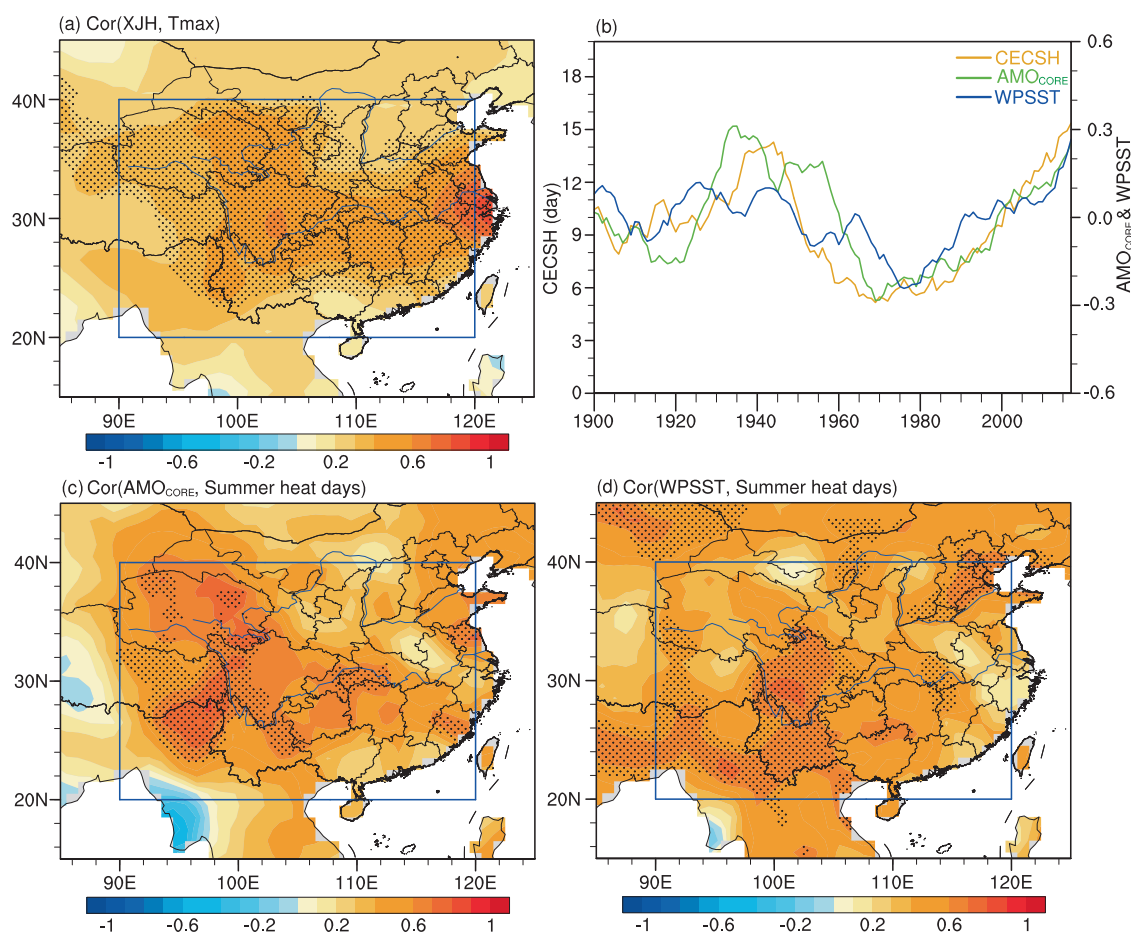


Fig. 1 | The time series of the CECSH, AMO_{CORE} and WPSST and their relationship. **a** Correlation of boreal summer-averaged daily maximum temperature in central-eastern China based on the Berkeley Earth data with that measured data from the Xujiahui Meteorological Observatory in Shanghai. The blue outline indicates the area of Central-eastern China (20°–40°N, 90°–120°E) in this study. **b** Sequences of the 11-year smoothed mean CECSH (yellow line; days), and

detrended AMO_{CORE} (green line; °C), WPSST (blue line; °C) anomalies in the boreal summer during the period 1900–2019. Correlation of boreal summer extreme heat days in central-eastern China with the detrended boreal summer **c** AMO_{CORE} and **d** WPSST anomalies after 11-year smoothed mean during the period 1900–2019. The black dot indicates the correlation coefficient above the 95% confidence interval based on effective degrees of freedom.

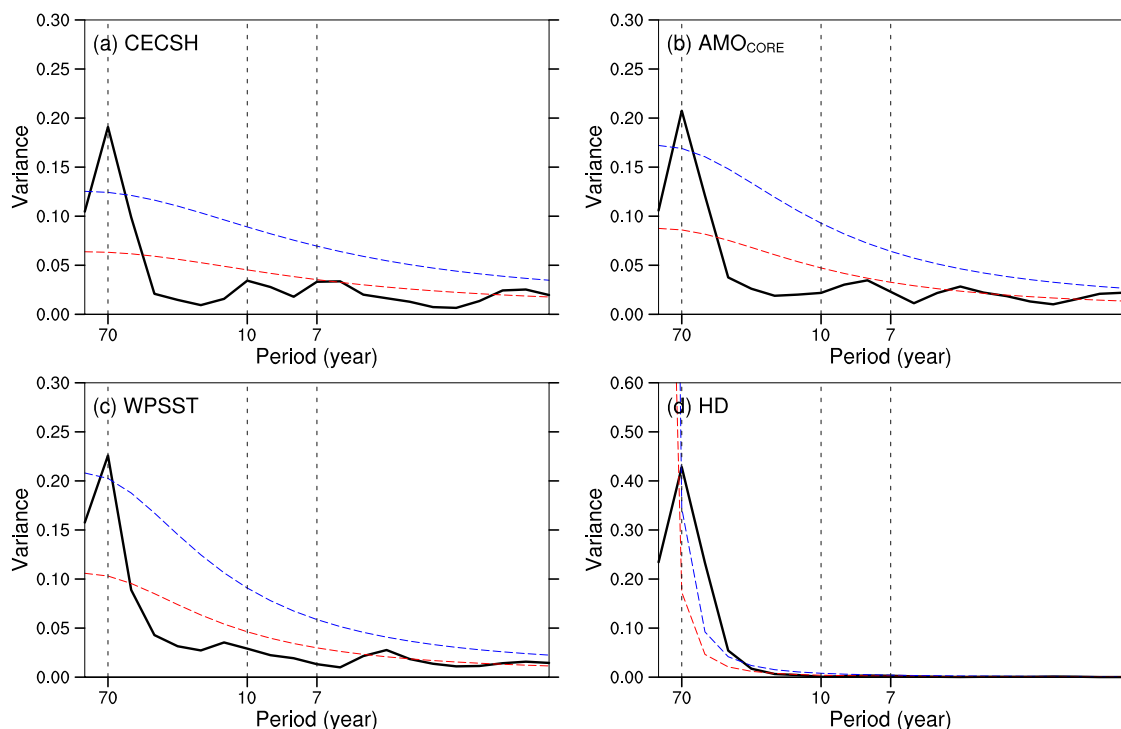


Fig. 2 | Continuous power spectrum of the CECSH, AMO_{CORE} , WPSST, and HD index. Continuous power spectrum of **a** CECSH (days) and detrended boreal summer **b** AMO_{CORE} , **c** WPSST for the period 1900–2019, and **d** HD indices for the

period 1900–2015. The dashed blue and red lines represent the confidence level at 90% and the reference red noise spectrum, respectively.

averaged daily maximum temperatures in most areas of the CEC based on the Berkeley Earth data have strong correlations with the measured data at the Xujiahui station in Shanghai, which verifies the reliability of the Berkeley Earth daily maximum temperatures in the CEC region. Meanwhile, the high correlation areas are mostly concentrated within the CEC, indicating that the summer-averaged daily maximum temperatures in the CEC region have better consistent change characteristics. Next, the Berkeley Earth data will be used to study the decadal variability of the CECSH.

As shown in Fig. 1b, the CECSH has an obvious decadal variability, with a mean value of 9.54 days from 1900 to 2019, roughly higher than the mean value during 1914 to 1951, lower than the mean value during 1952 to 1998, and higher than the mean value again during 1999 to 2019, showing a “more-less-more” decadal variation. Continuous power spectrum analysis shows that the decadal variability of the CECSH is approximately on a 70-year cycle and passes the significance test at the 90% confidence level (Fig. 2a). Although only nearly two cycles are covered from 1900 to 2019, previous studies^{42,45} have shown that annual mean, winter mean, and winter minimum temperatures in the CEC have similar decadal variability on a roughly 50–70-year cycle, supporting the plausibility of the CECSH having decadal variability on a roughly 70-year cycle. In addition, the continuous power spectrum of summer temperatures in the CEC also shows a decadal variability with a roughly 70-year cycle (figure not shown). The AMO_{CORE} and WPSST anomalies in boreal summer also show corresponding “positive-negative-positive” decadal variations as the CECSH (Fig. 1b), and the continuous power spectra of the AMO_{CORE} (Fig. 2b) and the WPSST (Fig. 2c) show that the detrended AMO_{CORE} and WPSST also have peaks at about 70 years, indicating that the decadal variability of both is also on a cycle of about 70 years, which is consistent with the cycle of decadal variability of the CECSH. These suggest that the decadal variability of the CECSH may have some connection with the AMO_{CORE} and the WPSST. In addition, it is well known that recent extreme summer heat, especially since the 21st century, has been influenced by more human activities than in the 1940s, and the coincidence of the AMO_{CORE} and WPSST with the CECSH of the 1940s

could also suggest that the AMO_{CORE} and WPSST do have an important influence on the CECSH.

Figure 1c, d shows the spatial correlations of the number of extreme summer heat days over the CEC with the detrended AMO_{CORE} and WPSST anomalies in boreal summer after an 11-year smoothed mean during the period 1900–2019. The summer AMO_{CORE} is correlated with the number of summer extreme heat days in the CEC region on the decadal timescale, especially in the west-central region, where the correlation coefficients of almost half of the regions pass the significance test at the 95% confidence level (Fig. 1c). Similarly, as shown in Fig. 1d, the summer WPSST is also correlated with the number of summer extreme heat days in the CEC on the decadal timescale. It should be noted that the relationship shown in Fig. 1c, d is not particularly strong, probably because the interdecadal variability of summer extreme heat in CEC may be synergistically influenced by the AMO_{CORE} and the WPSST, and the AMO_{CORE} or the WPSST alone do not fully correspond to the interdecadal variability of the CECSH. In addition, combining Fig. 1c, d, it can be found that the regions where the WPSST is significantly correlated with the number of summer extreme heat days in the CEC are to some extent spatially complementary to those where the AMO_{CORE} is significantly correlated, e.g., the AMO_{CORE} is significantly correlated with the number of summer extreme heat days in the regions of Qinghai and western Sichuan to eastern Tibet, and is somewhat correlated but not significantly correlated in the region of eastern Sichuan, while for the WPSST it is significantly correlated with the number of summer extreme heat days in the eastern Sichuan region, and somewhat correlated in the Qinghai region, but not significant. These results suggest that the decadal variability of summer extreme heat in the central-eastern region of China may be synergistically influenced by the AMO_{CORE} and the WPSST.

It should be noted that the AMO_{CORE} and the WPSST were studied as the main drivers of the decadal variability of CECSH as a result of attribution analyses, and it was found that the decadal variability of CECSH is mainly influenced by the AMO_{CORE} and the WPSST, but the influence of other

climatic factors on the CECSH cannot be excluded, especially on its annual variability.

Mechanisms by which the AMO_{CORE} and the WPSST influence the decadal variability of the CECSH

It was found above that the CECSH decadal variability may be influenced synergistically by the AMO_{CORE} and the WPSST. But how do the AMO_{CORE} and the WPSST synergistically influence the interdecadal variability of the CECSH? Based on the theory of the air-sea coupled bridge⁴⁶, SSTs, especially remote SSTs, influencing the regional climate are usually linked by an atmospheric bridge. In the case of extreme heat, its occurrence is inevitably directly influenced by local atmospheric changes such as subsidence warming, warm air transport, and radiation enhancement^{18,47–49}. Therefore, we conjecture that the AMO_{CORE} and the WPSST synergistically influence the local climate factor in the CEC through atmospheric bridges, which in turn influence the decadal variability of the CECSH. After a series of analyses, this conjecture is confirmed, and it is found that the AMO_{CORE} and the WPSST can synergistically form a local heat dome (HD) in the CEC, which in turn influences the decadal variability of the CECSH. A detailed description is given below.

CECSH decadal variability is directly influenced by the localized heat dome. Figure 3a, b show the spatial correlations of the 400 and 1000 hPa geopotential height anomalies over the CEC and its surroundings during boreal summer with the CECSH after an 11-year smoothed mean, respectively. It can be seen that the CECSH is significantly correlated with the geopotential height anomalies at 400 hPa in the region from Mongolia to northeastern China on the decadal timescale, and has a non-significant negative correlation with the geopotential height anomalies at 1000 hPa in the region of the CEC. As shown in Fig. 3c, d, the composites of the boreal summer geopotential height anomalies at 400 and 1000 hPa in the CECSH high-value year (above 9.5 days, which is the mean value of the CECSH from 1900 to 2019) on the decadal timescale also show a consistent result, suggesting that the decadal variability of the CECSH may be potentially related to the positive geopotential height anomalies at high levels located from Mongolia to northeastern China, which can be viewed as a HD for the CEC. HD is a phenomenon where high pressure at high altitude covers the ground like a dome and can cause the atmosphere near the surface to heat up dramatically⁵⁰. The ability of HDs to cause an increase in extreme heat, particularly as it has led to an increase in extreme heat in North America in recent years, has attracted increasing attention from researchers^{9,51–53}. Zhang et al.⁵³ point out that the impact of HDs on extreme heat, similar to that in North America in 2021, will increase in the future under a warming scenario. Liu et al.⁹ also point out that the historically extreme early summer heat in North China in 2023 is influenced by the HD, which is similar to that in Fig. 3. These suggest that the decadal variability of the CECSH may be under the direct influence of this localized HD.

Figure 4 explains the influence of this local HD on the CECSH by analyzing the horizontal and vertical temperature transport. Figure 4a shows the vertical distribution of the composite difference in the boreal summer horizontal temperature transport anomalies at the northern boundary (40°N) of the CEC during the high and low CECSH on the decadal timescale, and it can be seen that anomalous horizontal temperature transport to the south in the upper levels at and above 150 hPa, and to the north below this level, accompanied by anomalous vertical temperature transport down the CEC region (Fig. 4b). These results illustrate that this local HD can increase the summer extreme heat in the CEC region by compressing the atmosphere, triggering subsidence movements, and preventing cold air from entering the CEC region, which is also consistent with the mechanism by which HD affects extreme heats in the individual case studies⁹. In addition, it can also be found that the vertically reversed temperature advection patterns contribute to the establishment of a baroclinic configuration characterized by vertical wind shear and thermal gradients—key drivers of baroclinic instability. However, the subsidence observed

throughout the atmospheric column acts as a stabilizing mechanism, effectively suppressing the vertical coupling processes essential for baroclinic wave amplification and convective initiation.

Figure 5a shows the scatter plot of the CECSH versus the boreal summer HD index on the decadal timescale. It can be seen that the decadal CECSH has a good correspondence with the HD indices, when the HD indices are positive, the value of the decadal CECSH is also larger, when the HD indices are negative, the value of the decadal CECSH is smaller, and the correlation coefficient between the CECSH and the HD index reaches 0.8, and passes the significance test at the 95% confidence level based on the effective degrees of freedom. These further illustrate that the decadal variability of the CECSH is directly influenced by the localized HD here.

Relationship of the HD to the AMO_{CORE} and the WPSST and the underlying physical mechanism.

How do the HD relate to the AMO_{CORE} and the WPSST? Figure 5b, c show the scatter plot of the boreal summer HD index versus the boreal summer detrended AMO_{CORE} and WPSST anomalies after standardization, respectively. It can be seen that the HD index has a significant correspondence with both the AMO_{CORE} and the WPSST anomalies on the decadal timescale, and is generally positive when the AMO_{CORE} or WPSST is a positive anomaly, and negative otherwise. The correlation coefficients of the decadal AMO_{CORE} and WPSST anomalies with the HD index reached 0.65 and 0.73, respectively, and both passed the significance test with a confidence level of 95% based on the effective degrees of freedom. Figure 6 shows the correlation map of the boreal summer SST in the regions of the AMO_{CORE} and the tropical western Pacific with the boreal summer HD index on the decadal timescale. It can be seen that the HD index is also spatially significantly correlated with the SSTs over the AMO_{CORE} and the WPSST region, further suggesting that there may be a potential link between the HD with the AMO_{CORE} and the WPSST on the decadal timescale.

It should be noted that there are some HD indices that deviate from the fitted line when the standardized AMO_{CORE} is between -1 and 0 (Fig. 5b), and some HD indices that deviate from the fitted line when the standardized WPSST is between 0 and 1 (Fig. 5c), suggesting that the HD may not be influenced by the AMO_{CORE} or the WPSST alone. Figure 5d shows the correspondence between the HD index and the bifactor constructed by combining the AMO_{CORE} and the WPSST, and it can be seen that the relationship between the bifactor and the HD index is improved compared to either the AMO_{CORE} or the WPSST alone, the correlation coefficient reaches 0.78, exceeding the correlation with either the AMO_{CORE} or the WPSST alone. These results indicate that the HD is not influenced by the AMO_{CORE} or the WPSST alone, but rather by the synergistic influence of the AMO_{CORE} and the WPSST.

In order to identify the mechanisms by which the AMO_{CORE} and the WPSST influence the local HD, the decadal relationship between the HD index and the geopotential height anomalies at different levels was analyzed. Figure 7 shows the correlation map of 400, 600, 800, and 1000 hPa geopotential height anomalies in the boreal summer across the North Atlantic to East Asia on the decadal timescale. It can be seen that the geopotential height anomalies in the mid- to high-latitude regions of the North Atlantic have a significant negative correlation with the HD index and gradually weaken with increasing height, while in the Mediterranean Sea to East European regions the correlation shifts from negative in the lower levels to positive in the upper levels and gradually strengthen with increasing height. This suggests that the AMO_{CORE} may propagate downstream to the East Asian region at about 400 hPa by stimulating such local convection, which has been pointed out by researchers in previous studies^{54,55}. In the Mongolia-Northeast China region, the positive correlation between geopotential height anomalies and the HD index gradually increases from lower to higher levels, suggesting that the WPSST may produce a similar anomalous geopotential height field at about 400 hPa by stimulating convection.

To further reveal the mechanism by which the AMO_{CORE} and the WPSST synergistically influence the localized HD on the decadal

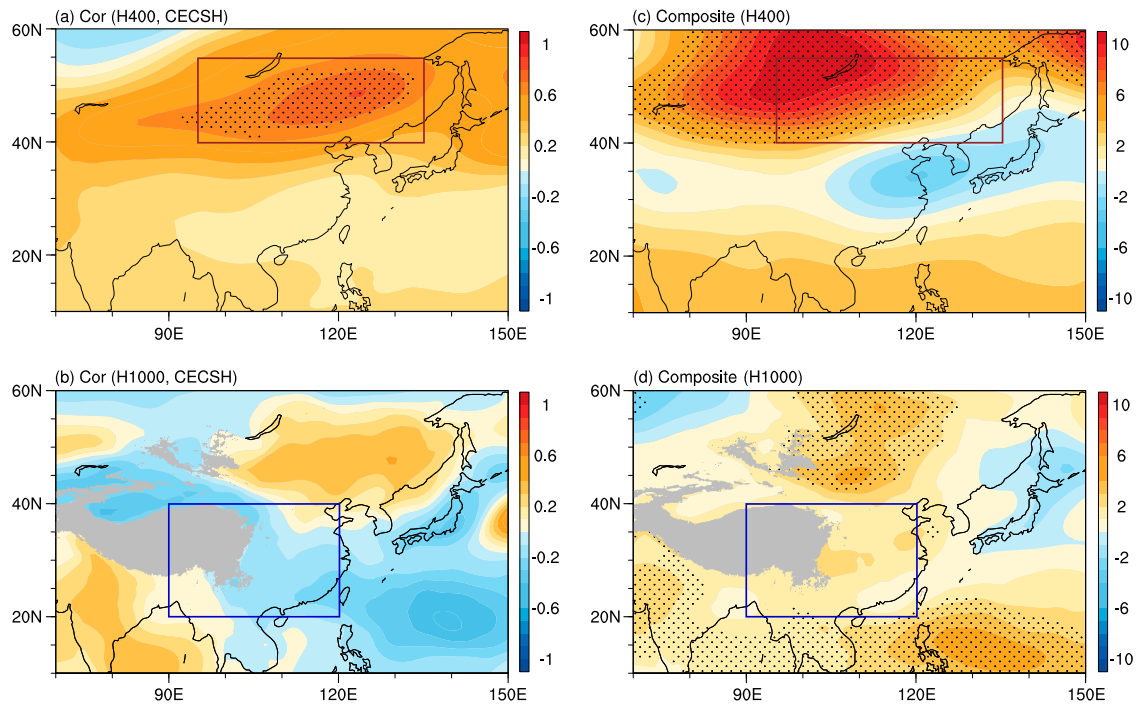
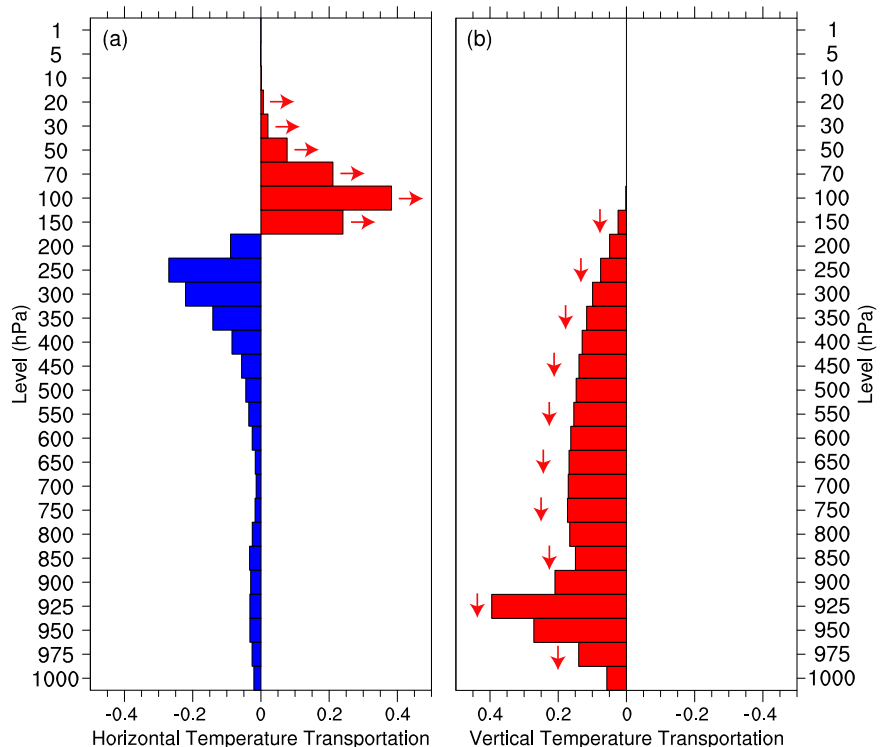


Fig. 3 | Local geopotential height anomalies according to the CECSH. Correlation of the boreal summer geopotential height anomalies at **a** 400 hPa and **b** 1000 hPa with the CECSH after 11-year smoothed mean for the period 1900–2015. The black dot indicates the correlation coefficient above the 90% confidence interval based on effective degrees of freedom. The red outline indicates the dome position (40°–45°N,

95°–135°E) of the HD index. Grey areas indicate the areas of high elevation. Composites of the boreal summer geopotential height anomalies (gpm) at **c** 400 hPa and **d** 1000 hPa in the CECSH high-value year (above 9.5 days) on the multidecadal timescale for the period 1900–2015. The black dot indicates the anomalies above the 99% confidence interval.

Fig. 4 | Vertical and horizontal temperature transport according to the CECSH. **a** Vertical distribution of the composite difference in the boreal summer horizontal temperature transportation anomalies at the northern boundary (40°N) of central-eastern China during the high and low CECSH on the decadal timescale during the period 1900–2015. The high and low CECSH refer to the number of days above and below the mean value of 9.54 days between 1900 and 2019, respectively. Southward transport is defined as positive (red bar), and northward transport is defined as negative (blue bar). **b** As in (a), but for the vertical temperature transportation anomalies, and the downward transport is defined as positive (red bar).



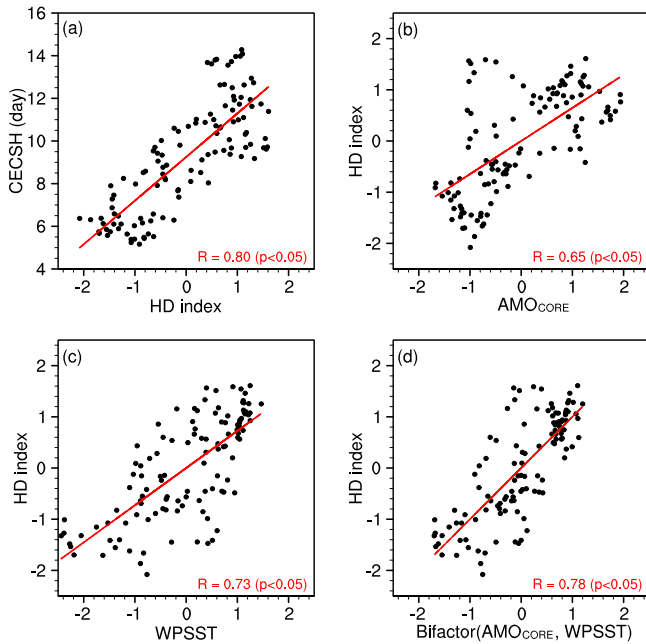


Fig. 5 | Scatter plots of the CECSH for the HD index, the HD index for the AMO_{CORE} and the WPSST. **a** Scatter plot of the CECSH versus the boreal summer HD index on the decadal timescale during the period 1900–2015. The red line is the linear fit. R and p indicate the correlation coefficient and its p value. **b, c** As in (a), but for the boreal summer HD index versus the boreal summer detrended AMO_{CORE} and WPSST anomalies after standardization, respectively. **d** Also similar to (a), but for the boreal summer HD index versus the bifactor based on the AMO_{CORE} and WPSST anomalies.

timescale, the synergistic diagnostic results are displayed in Fig. 8. As shown in Fig. 8a, when both the decadal AMO_{CORE} and WPSST anomalies are in the negative phase during the boreal summer, the 400h Pa level over Mongolia to northeast China represented negative geopotential height field anomalies, which were unfavourable for the generation of the localized HD. Also, when the decadal AMO_{CORE} is in positive phase and the decadal WPSST is not (Fig. 8b), and when the decadal WPSST is in positive phase and the decadal AMO_{CORE} is not (Fig. 8c), there are no consistent positive geopotential height anomalies at 400 hPa from Mongolia to northeast China, suggesting that neither the AMO_{CORE} alone nor the WPSST alone is capable of generating the localized HD. The anomalous positive geopotential height at 400 hPa occurs from Mongolia to northeast China when both the decadal AMO_{CORE} and the decadal WPSST are in positive phase. These results confirm that the localized HD is synergistically influenced by the AMO_{CORE} and the WPSST.

Then, the roles of the AMO_{CORE} and the WPSST in synergistically influencing the local HD were analyzed by performing linear baroclinic model (LBM) experiments, respectively. As shown in Fig. 9, the AMO_{CORE} is capable of inducing positive geopotential height anomalies at mid to low latitudes in the North Atlantic, especially negative geopotential height anomalies at mid to high latitudes in the North Atlantic, and positive geopotential height anomalies in the Mediterranean Sea to Eastern Europe, all of which increase progressively with increasing height, corresponding to the circulation in Fig. 7. This further confirms that the AMO_{CORE} can influence the localized HD by triggering the above circulation and its downstream propagation. As shown in Fig. 10, warm SSTs in the tropical western Pacific can stimulate positive geopotential height anomalies, and the center of the positive geopotential height anomalies gradually extends to the northwest and strengthens with increasing height, corresponding to the circulation in Fig. 7, confirming that the WPSST can stimulate the above circulation and impede the downstream movement of the AMO_{CORE} -

induced circulation, resulting in atmospheric buildup in the region from Mongolia to northeastern China, which leads to the formation of the localized HD.

Mechanism-based empirical model for the decadal variability of the CECSH

Here, empirical models of the decadal variability of the CECSH are constructed with mechanistic underpinnings based on the AMO_{CORE} and the WPSST, respectively. The empirical model based on the AMO_{CORE} is as follows:

$$\text{Decadal } \tilde{CECSH}_1(t) = a_1 * \text{Decadal } AMO_{CORE}(t) + c_1 * t + e_1 \quad (1)$$

and the empirical model based on the WPSST is as follows:

$$\text{Decadal } \tilde{CECSH}_2(t) = a_2 * \text{Decadal } WPSST(t) + c_2 * t + e_2 \quad (2)$$

where t is time for year, the coefficients a_1 , c_1 and a_2 , c_2 are obtained by minimizing the root mean square error based on the corresponding multiple linear regression, respectively, e_1 and e_2 are the corresponding remaining residual terms.

As shown in Fig. 11a, b, the empirical models constructed on the basis of the AMO_{CORE} and the WPSST alone are both able to reproduce the decadal variability of the CECSH, with observed values almost exclusively within the 2- sigma uncertainty of the modelled values. And the correlation coefficients between the two modeled CECSH and the observations reached 0.78 and 0.80, respectively, and the corresponding root mean square errors were 1.78 and 1.71. Nevertheless, it should be noted that both models have certain limitations, e.g., the AMO_{CORE} -based model simulates a peak that does not correspond to the observed peak around 1945 and under-simulates the rapid increase of the decadal CECSH since 2010, while the WPSST-based model under-simulates the peak intensity of the decadal CECSH around 1945.

$$\text{Decadal } \tilde{CECSH}_3(t) = a_3 * \text{Decadal } AMO_{CORE}(t) + b_3 * \text{Decadal } WPSST(t) + c_3 * t + e_3 \quad (3)$$

As shown in Fig. 11c, the empirical model (Eq. 3) constructed based on the synergistic effects of the AMO_{CORE} and the WPSST is able to significantly improve the simulation capability of the decadal CECSH, with the correlation coefficient between the observed and modeled decadal CECSH improving to 0.88 and the root mean square error reducing to 1.36. The model not only reduced the uncertainty in its predictions, but was also able to simulate the peak of decadal CECSH around 1945 and the rapid increase from 2010. In addition, it is also confirmed again that the decadal variability of the CECSH is synergistically influenced by the AMO_{CORE} and the WPSST.

Hindcast experiments were conducted to check the predictive performance of the decadal CECSH empirical model. As shown in Fig. 12, hindcast experiments based on constructing the model over different periods of time, as well as different prediction horizons, are shown to demonstrate the stability of the decadal CECSH model. Figure 12a gives a hindcast experiment based on data from 1900 to 1995 modelled for the decadal CECSH from 1996 to 2000. It can be seen that the empirical model is able to predict the 1996–2000 decadal CECSH relatively well. Similarly, Fig. 12b gives a hindcast experiment based on data from 1900 to 2014 modelled for the decadal CECSH from 2015 to 2019. Figure 12c also shows a hindcast of the decadal CECSH for the following 10 years (2010 to 2019) based on modelling from 1900 to 2009. It can be seen that the hindcasted decadal CECSH of the empirical model reproduces the observed CECSH well, indicating that the empirical model has good stability, and further indicating that the synergistic effect of the AMO_{CORE} and the WPSST on the decadal CECSH is stable.

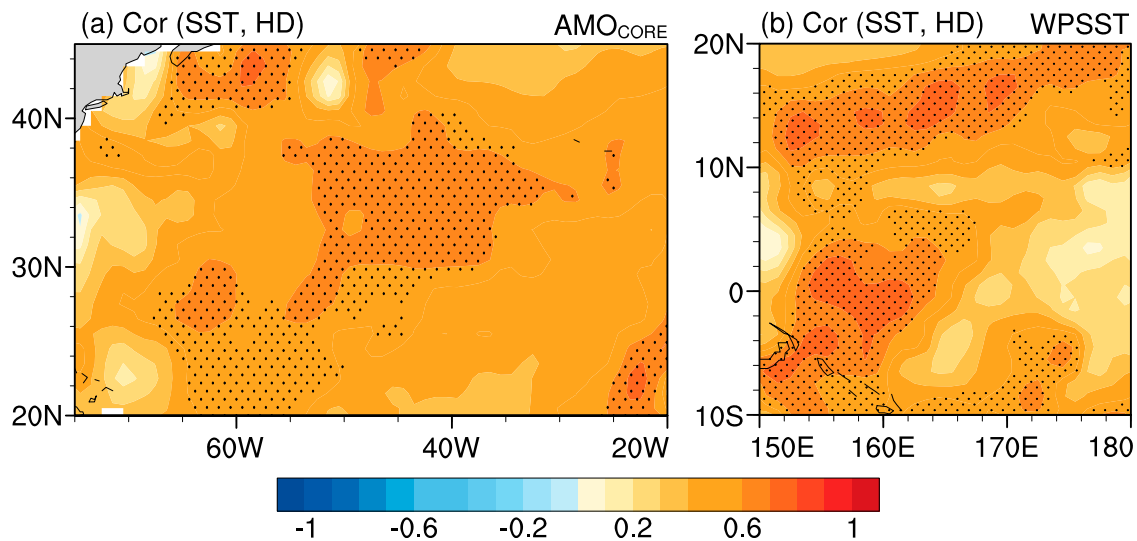


Fig. 6 | Relationship of the CECSH with the AMO_{CORE} and the WPSST. Correlation of the boreal summer SST in the regions of **a** the AMO_{CORE} (20°–45°N, 75°–20°W) and **b** the tropical western Pacific (10°S–20°N, 150°–180°E) with the

boreal summer HD index on the decadal timescale during the period 1900–2015. The black dot indicates the significance of the correlation coefficient above the 90% confidence interval based on effective degrees of freedom.

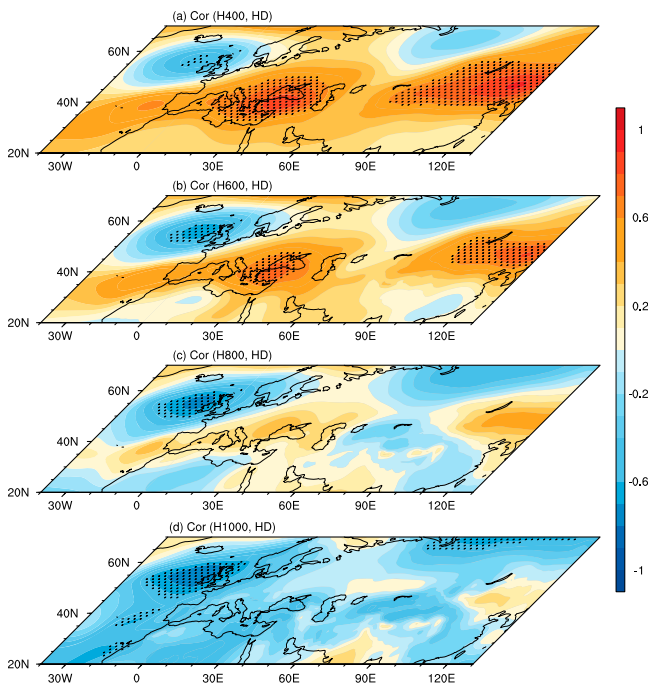


Fig. 7 | Relationship of the HD index with geopotential height anomalies. Correlation of **a** 400 hPa, **b** 600 hPa, **c** 800 hPa, and **d** 1000 hPa geopotential height anomalies in the boreal summer in the North Atlantic to East Asia on the decadal timescale during the period 1900–2015. The black dot indicates the significance of the correlation coefficient above the 90% confidence interval.

Conclusion and discussion

In this study, the synergistic effects of the AMO_{CORE} and the WPSST on the decadal variability of the CECSH are investigated, revealing the physical mechanism that the AMO_{CORE} and the WPSST generate the localized HD in the CEC through synergistic interaction, which in turn influences the decadal CECSH, and constructs the empirical model of the decadal CECSH, which has a physical basis and is well simulated, based on the AMO_{CORE} and the WPSST.

In particular, the decadal variability of the CECSH is first analyzed based on long time-series data, and it is found that the decadal variability of

the CECSH has a roughly 70-year cycle and is significantly related to the North Atlantic SST (here defined as the AMO core area SST, AMO_{CORE}) and the tropical western Pacific SST (here defined as the WPSST). Secondly, the local circulation corresponding to the decadal variability of the CECSH is investigated, and it is found that the decadal variability of the CECSH is directly influenced by the localized HD, whose upper level is located from Mongolia to northeast China and the lower level is located in the CEC. Thirdly, we propose and verify the mechanism hypothesis that the AMO_{CORE} and the WPSST synergistically influence the decadal CECSH through the aforementioned local HD. It is found that the AMO_{CORE} can excite positive geopotential height anomalies at mid to high latitudes in the North Atlantic and from the Mediterranean Sea to Eastern Europe, and produce negative geopotential height anomalies at mid to low latitudes in the North Atlantic, and both gradually intensify with increasing heights, and are transported downstream at high altitudes around 400 hPa. The WPSST can produce positive geopotential height anomalies in the tropical western Pacific that gradually increase and extend north-westward with increasing height, hindering upstream atmospheric movement and leading to atmospheric accretion in Mongolia to northeast China, forming the localized HD. This means that the synergistic effects of the AMO_{CORE} and the WPSST favor the formation of the local HD that can influence the CECSH decadal variability. Finally, the empirical models of the decadal CECSH are constructed based on the AMO_{CORE} or the WPSST alone, and based on the synergistic effects of the AMO_{CORE} and the WPSST, respectively, and it is found that the empirical model constructed based on the synergistic effects of the AMO_{CORE} and the WPSST can significantly improve the simulation ability of the CECSH decadal variability. Hindcast experiments further confirmed that the empirical model of the decadal CECSH constructed from the AMO_{CORE} and the WPSST has a good prediction performance.

The SST has better persistence relative to air temperature and circulation, so it can be used to predict the decadal CECSH, but we construct an empirical model for the CECSH based on the AMO_{CORE} and the WPSST in the same summer, so if it is to be better applied in climate prediction operations, the predictive ability of the dynamical climate model to predict the AMO_{CORE} and the WPSST needs to be assessed and objectively revised. Senapati et al.⁴³ found that positive SST anomalies in the Atlantic tropics can weaken the trade winds during the summer, leading to a shallower mixed layer and lower heat capacity, which in turn affects the SST in the mid to high latitudes of the North Atlantic, and thus the influence of Atlantic tropical SST on the CECSH can be explored in terms of a leading effect to obtain its forecast signals, which is worth a new study in the future. In

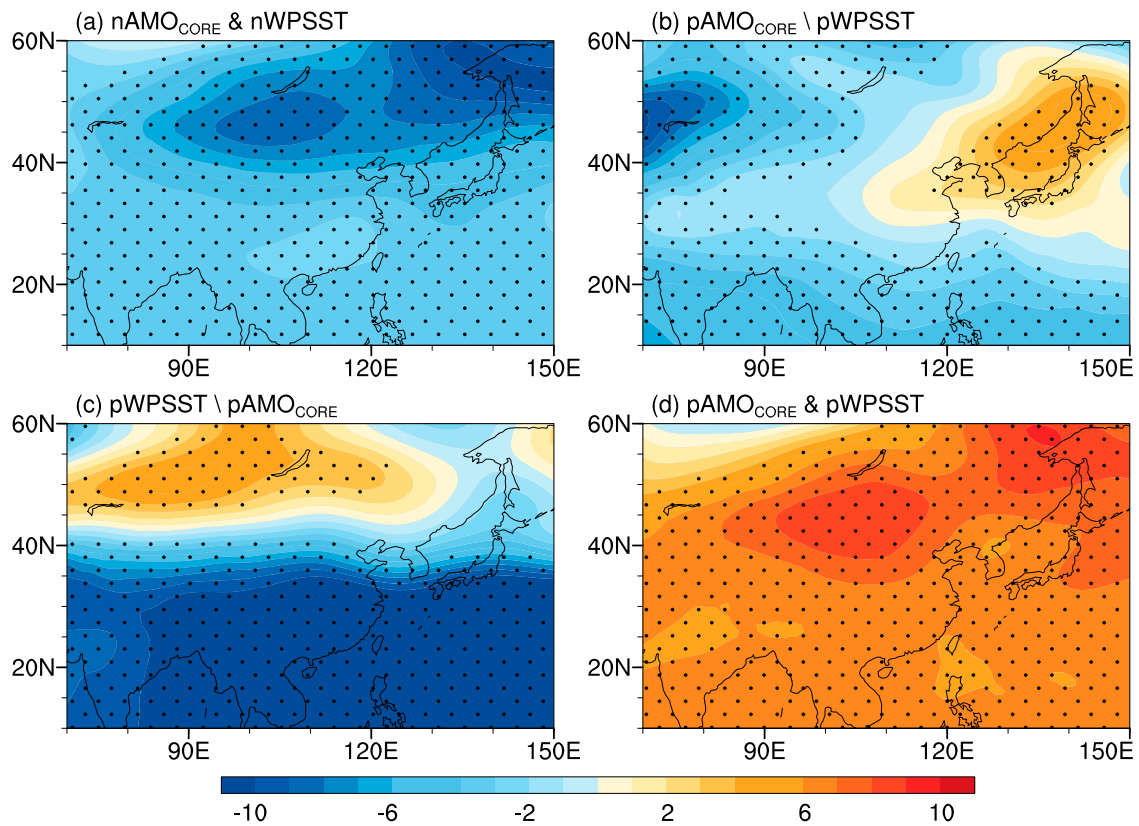


Fig. 8 | Composite of the geopotential height anomalies. **a** Composites of the boreal summer 400 hPa geopotential height anomalies in the East Asia for the joint occurrence of negative AMO_{CORE} ($nAMO_{CORE}$) and negative WPSST ($nWPSST$) anomalies ($nAMO_{CORE}$ and $nWPSST$) after detrending on the decadal timescale during the period 1900–2015. The black dot indicates the anomalies above the 90% confidence interval. **b, c, d** As in (**a**), but for the joint occurrence of positive

AMO_{CORE} ($pAMO_{CORE}$) and non-positive WPSST ($pWPSST$) anomalies ($pAMO_{CORE} \setminus pWPSST$), positive WPSST ($pWPSST$) and non-positive AMO_{CORE} ($pAMO_{CORE}$) anomalies ($pWPSST \setminus pAMO_{CORE}$), and positive AMO_{CORE} ($pAMO_{CORE}$) and positive WPSST ($pWPSST$) anomalies ($pAMO_{CORE}$ and $pWPSST$), respectively. Non-positive includes negative anomalies and anomalies of 0.

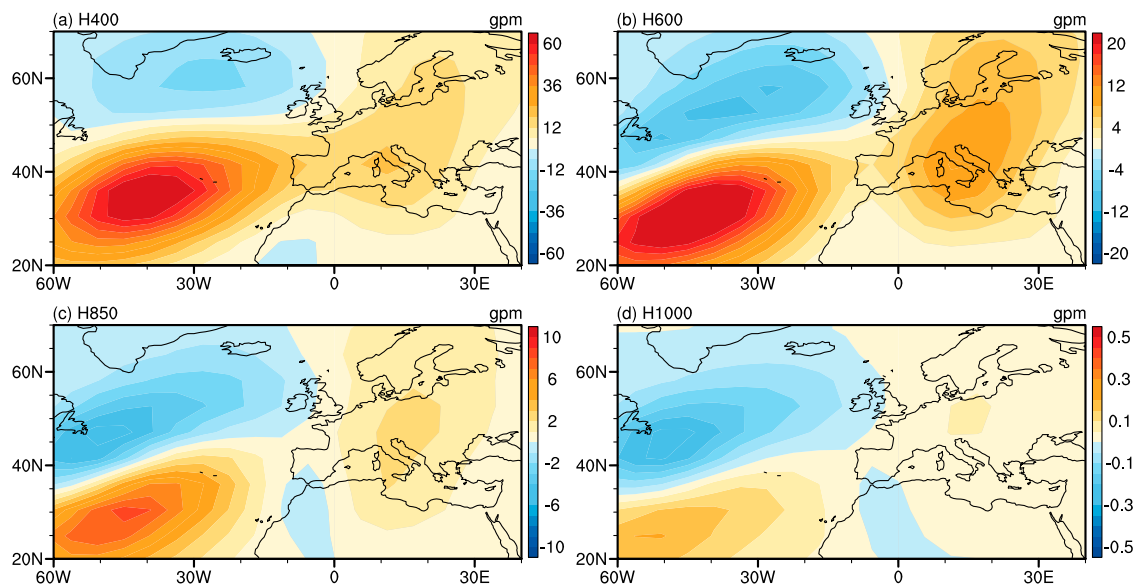


Fig. 9 | LBM experiment in accordance with the AMO_{CORE} . The **a** 400 hPa, **b** 600 hPa, **c** 850 hPa, and **d** 1000 hPa geopotential height anomalies derived from LBM with the boreal summer background conditions and the thermal forcing sources localised as the positive AMO_{CORE} pattern.

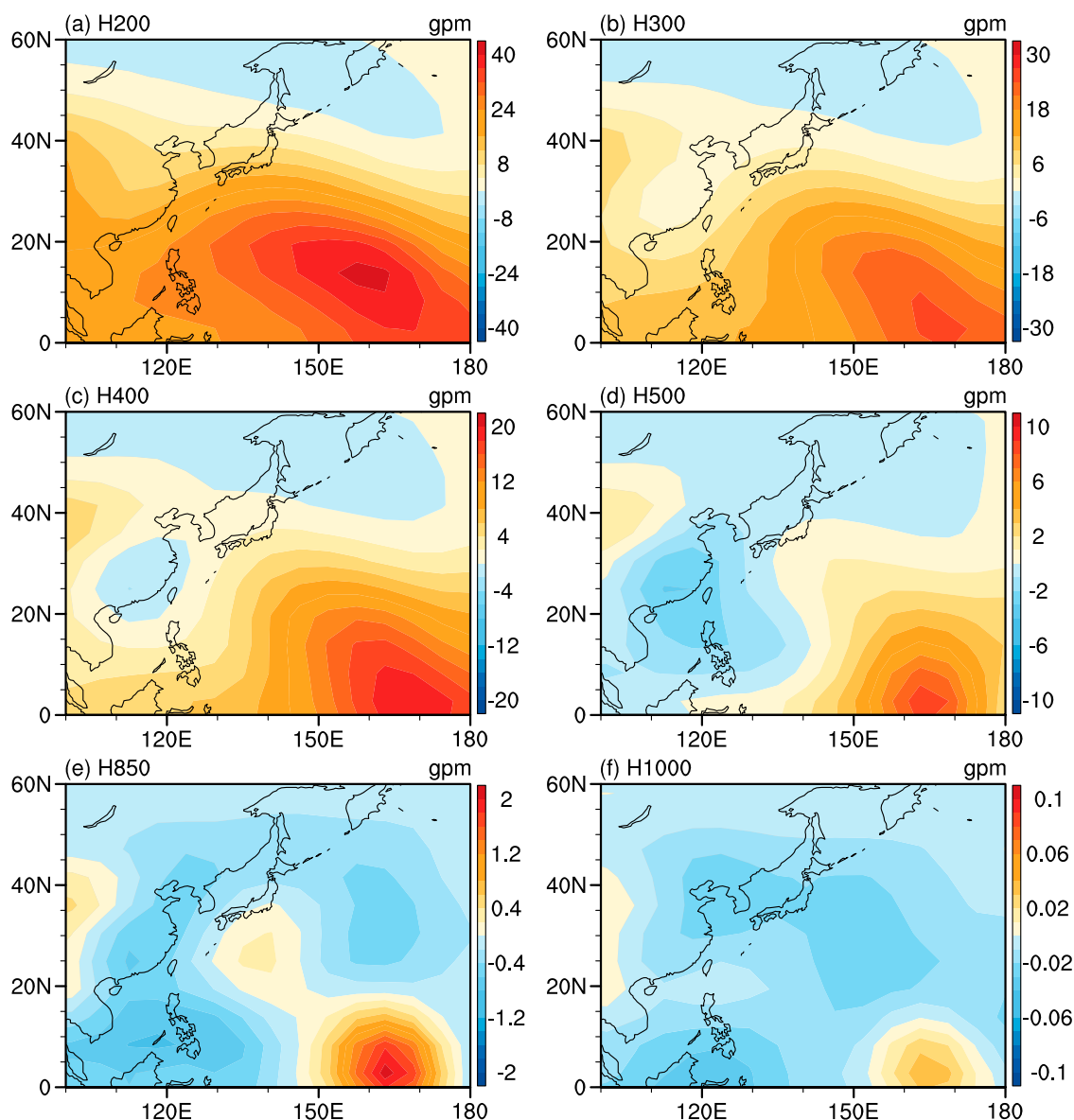


Fig. 10 | LBM experiment in accordance with the WPSST. The a 200 hPa, b 300 hPa, c 400 hPa, d 500 hPa, e 850 hPa, and f 1000 hPa geopotential height anomalies derived from LBM with the boreal summer background conditions and the thermal forcing sources localised as the positive WPSST pattern.

addition, we only analyzed the synergistic effects of the AMO_{CORE} and the WPSST on the decadal variability of the CECSH, and there may be other climatic factors that can synergistically influence the CECSH, which also need to be further investigated in the future. Della-Marta et al.⁵⁶ pointed out that peaks of summer extreme heat were also observed in Europe in the 1930s to 1940s, and that the decadal variability of summer extreme heat needs to be regrouped in the future from a global perspective.

Methods

Observational data

Daily maximum temperatures (T_{max}) were obtained from the Berkeley Earth dataset⁵⁷, covering the period 1880–present, with a horizontal resolution of 1° latitude \times 1° longitude, which can well characterize the daily maximum temperature in the CEC. Measured temperatures from the Xujiahui meteorological observatory in Shanghai from 1873 to the present were used to evaluate the effectiveness of the Berkeley Earth dataset in characterizing the maximum temperature of the CEC. Monthly SSTs were obtained from the Hadley Centre Sea Ice and SST (HadISST) dataset⁵⁸, which covers the period 1870–present and is at a horizontal resolution of 1° latitude \times 1° longitude. Monthly geopotential heights, temperatures,

horizontal and vertical winds at 1000 to 1 hPa pressure levels were obtained from the NOAA-CIRES-DOE 20th Century Reanalysis V3 (20CRv3)⁵⁹, which covers the period 1836–2015 and has a horizontal resolution of 1° latitude \times 1° longitude.

Definitions and indices

In this study, summer refers to the June–July–August. Extreme heat is defined by a relative threshold of 90 percent, meaning the daily maximum temperature above the 90th percentile defines an extreme heat day. It should be noted that for each calendar day during the summer of 1900–2019, we calculated the 90th percentile threshold of daily T_{max} at individual grid points through a ranking analysis, where daily T_{max} values exceeding the local threshold were classified as extreme heat days. The Central-eastern China is defined as the area of 20° – 40° N, 90° – 120° E, which is framed in Fig. 1a. The CECSH is calculated by a regional weighted average of the number of summer extreme heat days in Central-eastern China. The AMO_{CORE} is defined as the regionally weighted average SST in the AMO core area (20° – 45° N, 75° – 20° W), and the WPSST is defined as the regionally weighted average SST in the tropical western Pacific (10° S– 20° N, 150° – 180° E), framed in Fig. 6a, b, respectively. The bifactor

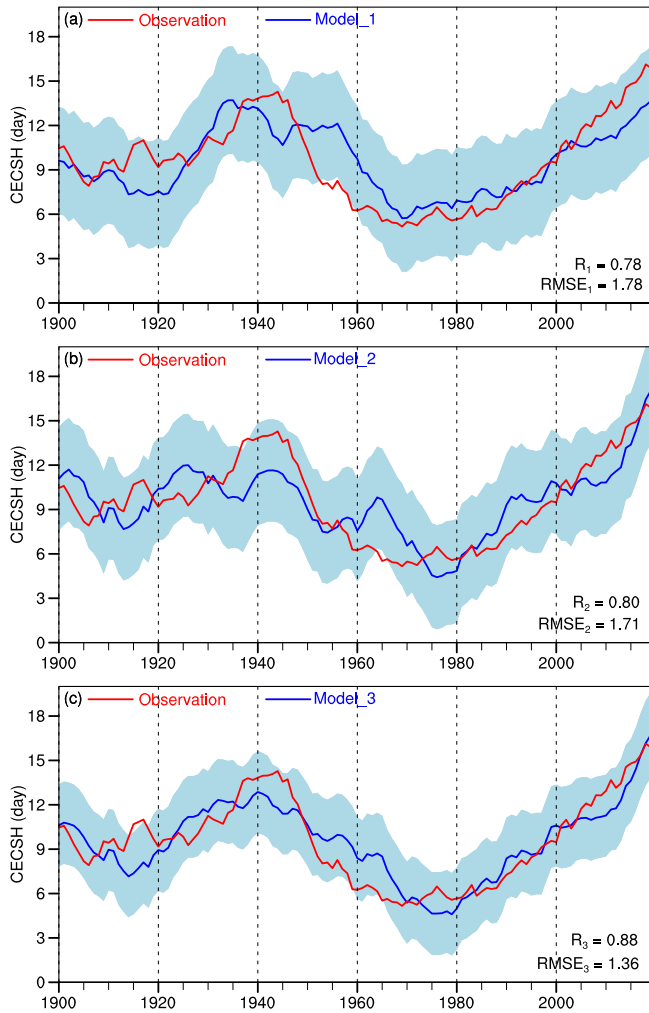


Fig. 11 | Empirical models of the decadal CECSH. Observed decadal CECSH (red line) and modeled decadal CECSH (blue line) based on the boreal summer decadal **a** AMO_{CORE} and **b** WPSST for the period 1900–2019, respectively. The shaded area in light blue marks the 2-sigma uncertainty range of the modeled values. **c** As in (a), but the modeled decadal CECSH based on the combined influence of the decadal AMO_{CORE} and the decadal WPSST.

(AMO_{CORE}, WPSST) corresponding to the CECSH was calculated by first regressing the CECSH on the AMO_{CORE} and WPSST by multiple linear regression to obtain the corresponding weight coefficients of the AMO_{CORE} and WPSST, and then multiplying the AMO_{CORE} and WPSST by their respective weight coefficients and summing to obtain the sum. The intensity of the heat dome (HD) is expressed by the difference between the 400 hPa geopotential height anomalies in the Mongolia to Northeast China (M-NC; 40°–45°N, 95°–135°E) and the 1000 hPa geopotential height anomalies in the Central-eastern China (CEC), and the HD index is calculated as follows:

$$HD\ index(t) = \frac{H400_{M-NC}(t) - H1000_{CEC}(t)}{2} \quad (4)$$

where t denotes year, $H400_{M-NC}$ denotes the regionally weighted average 400 hPa geopotential height anomalies in the M-NC region, and $H1000_{CEC}$ denotes the regionally weighted average 1000 hPa geopotential height anomalies in the CEC region. It should be noted that our analyses showed that the HD index based on the difference in geopotential height anomalies at 300 or 500 hPa versus 1000 hPa is insensitive to the results compared to the index derived based on 400, and 400 hPa was chosen to calculate and

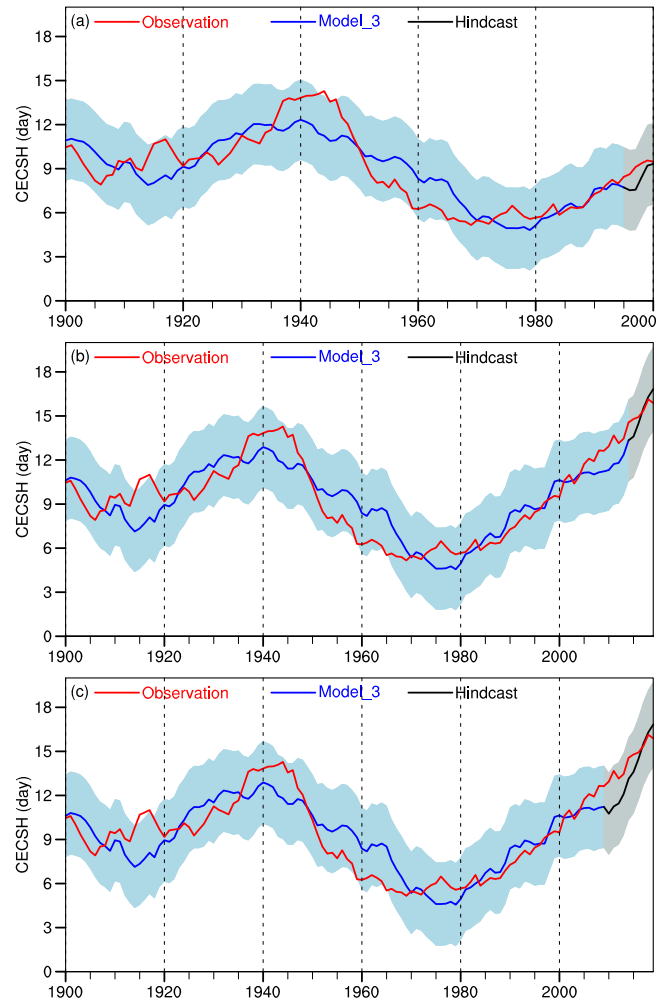


Fig. 12 | Hindcast tests of the decadal CECSH empirical model. Observed (red line), model (blue line), and hindcasted (black line) decadal CECSH. **a** Hindcast for the 1996–2000 decadal CECSH based on the model constructed with the AMO_{CORE} and WPSST for the period 1900–1995. The shaded area in light blue (black) marks the 2-sigma uncertainty range of the modeled (hindcast) values. **b** As in (a), but for the hindcast for the 2015–2019 decadal CECSH, based on a model constructed for the period 1900–2014. **c** As in (a), but for the hindcast for the 2010–2019 decadal CECSH, based on a model constructed for the period 1900–2009.

analyze because it has the strongest relationship with the CECSH relative to layers such as 300 and 500 hPa (not shown here).

The thermodynamic perturbation equation

Horizontal and vertical temperature transport are calculated using the following thermodynamic perturbation equations:

$$\frac{\partial T'}{\partial t} = - \left(u' \frac{\partial \bar{T}}{\partial x} + v' \frac{\partial \bar{T}}{\partial y} + \bar{u} \frac{\partial T'}{\partial x} + \bar{v} \frac{\partial T'}{\partial y} \right) + \frac{R(\gamma_d - \gamma)}{pg} (w' \bar{T} + \bar{w} T') \quad (5)$$

where \bar{T} (unit: K) is the temperature at the reference state, T' (unit: K) is the departure of the air temperature, \bar{u} (unit: $m\ s^{-1}$), \bar{v} (unit: $m\ s^{-1}$), \bar{w} (unit: $m\ s^{-1}$) are the latitudinal, meridional and vertical winds at the reference state, respectively, the u' (unit: $m\ s^{-1}$), v' (unit: $m\ s^{-1}$), w' (unit: $m\ s^{-1}$) are the corresponding departures, x (unit: m) and y (unit: m) are distances in the latitudinal and longitudinal directions, respectively, R ($287\ J\ kg^{-1}\ K^{-1}$) is the gas constant of dry air, γ_d and γ are the dry adiabatic lapse rate and the real atmospheric lapse rate, p is the pressure, g ($9.806\ m\ s^{-2}$) is the acceleration due to gravity.

The synergistic effect diagnostic method

The synergistic diagnostic method used here^{45,60} allows the presence of synergistic effects to be determined statistically. Suppose there are two forcing factors F_1 and F_2 , which can be divided into positive (pF_1 or pF_2) and negative (nF_1 or nF_2) respectively. When both forces are in the positive phase, they can be expressed as pF_1 & pF_2 , when both forces are in the negative phase, it is expressed as nF_1 & nF_2 . If F_1 is in positive phase and F_2 is not, it can be expressed as $F_1 \setminus F_2$, if F_2 is in positive phase and F_1 is not, it can be expressed as $F_2 \setminus F_1$. If the response T is investigated in this study, the difference between different events can be compared to see if there is a synergistic effect.

The linear baroclinic model

The linear baroclinic model (LBM) developed by Watanabe and Kimoto⁶¹ was applied to investigate the impact of the AMO_{CORE} and WPST on the CECSH. A dry version of the LBM and the summertime climatology with T21 horizontal resolution and 20 vertical layers derived from the ERA reanalysis dataset were used in this study. The LBM was integrated for 29 d and the results after stabilization were used. More details on the LBM can be obtained from Watanabe and Kimoto⁶¹.

In addition, the test of significance used in this study was student's t -test, and the degrees of freedom of the series after the smoothing filter may decrease, so the effective degree of freedom was used in the test of significance. The detrending in the article is to remove the linear trend, unless otherwise stated. Continuous power spectrum analysis and correlation analysis were also utilized in this study and will not be described in detail here.

Data availability

Berkeley Earth dataset is available at <https://www.berkeleyearth.org/data/>; HadISST is available at <https://www.metoffice.gov.uk/hadobs/hadisst/data/download.html>; 20CRv3 is available at https://psl.noaa.gov/data/gridded/data.20thC_ReanV3.html; The measured daily maximum temperatures from the Xujiahui meteorological observatory in Shanghai can be obtained by contacting the author.

Code availability

The LBM code is available at https://ccsr.aori.u-tokyo.ac.jp/~lbn/sub/lbn_4.html; All other codes involved in this study are based on NCL and can be available by contacting the author.

Received: 10 September 2024; Accepted: 14 May 2025;

Published online: 27 May 2025

References

- Russo, S. et al. Magnitude of extreme heat waves in present climate and their projection in a warming world. *J. Geophys. Res. Atmos.* **119**, 12500–12512 (2014).
- Bieli, M., Pfahl, S. & Wernli, H. A Lagrangian investigation of hot and cold temperature extremes in Europe. *Q. J. R. Meteorol. Soc.* **141**, 98–108 (2015).
- Fragkoulidis, G., Wirth, V., Bossmann, P. & Fink, A. Linking northern hemisphere temperature extremes to Rossby wave packets. *Q. J. R. Meteorol. Soc.* **144**, 553–566 (2018).
- Zhang, R. N., Sun, C. H., Zhu, J. S., Zhang, R. H. & Li, W. J. Increased European heat waves in recent decades in response to shrinking Arctic sea ice and Eurasian snow cover. *npj Clim. Atmos. Sci.* **3**, 7 (2020).
- Wang, J. & Yan, Z. W. Rapid rises in the magnitude and risk of extreme regional heat wave events in China. *Weather Clim. Extremes* **34**, 100379 (2021).
- Tang, S. et al. Linkages of unprecedented 2022 Yangtze River Valley heatwaves to Pakistan flood and triple-dip La Niña. *npj Clim. Atmos. Sci.* **6**, 44 (2023).
- White, R. H. et al. The unprecedented Pacific Northwest heatwave of June 2021. *Nat. Commun.* **14**, 727 (2023).
- Hotz, B., Papritz, L. & Röthlisberger, M. Understanding the vertical temperature structure of recent record-shattering heatwaves. *Weather Clim. Dynam.* **5**, 323–343 (2024).
- Liu, B. Q., Duan, Y. N., Ma, S. M., Yan, Y. H. & Zhu, C. W. Unconventional cold vortex as precursor to historic early summer heatwaves in North China 2023. *npj Clim. Atmos. Sci.* **7**, 167 (2024).
- Van Loon, S. & Thompson, D. W. J. Comparing local versus hemispheric perspectives of extreme heat events. *Geophys. Res. Lett.* **50**, e2023GL105246 (2023).
- Yule, E. L., Hegerl, G., Schurer, A. & Hawkins, E. Using early extremes to place the 2022 UK heat waves into historical context. *Atmos. Sci. Lett.* **24**, e1159 (2023).
- Zachariah, M. et al. Attribution of 2022 early-spring heatwave in India and Pakistan to climate change: lessons in assessing vulnerability and preparedness in reducing impacts. *Environ. Res. Clim.* **2**, 045005 (2023).
- Kornhuber, K. et al. Extreme weather events in early summer 2018 connected by a recurrent hemispheric wave-7 pattern. *Environ. Res. Lett.* **14**, 054002 (2019).
- Agel, L., Barlow, M., Skinner, C., Colby, F. & Cohen, J. Four distinct Northeast US heat wave circulation patterns and associated mechanisms, trends, and electric usage. *npj Clim. Atmos. Sci.* **4**, 31 (2021).
- Heeter, K. J. et al. Unprecedented 21st century heat across the Pacific Northwest of North America. *npj Clim. Atmos. Sci.* **6**, 5 (2023).
- IPCC, Climate Change 2023: Synthesis Report. Contribution of Working Groups I, II and III to the Sixth Assessment Report of the Intergovernmental Panel on Climate Change. (2023).
- Ma, F. & Yuan, X. When will the unprecedented 2022 summer heat waves in Yangtze River Basin become Normal in a warming climate? *Geophys. Res. Lett.* **50**, e2022GL101946 (2023).
- Xie, T. J. et al. Weather pattern conducive to the extreme summer heat in North China and driven by atmospheric teleconnections. *Environ. Res. Lett.* **18**, 104025 (2023).
- Zhang, T. T., Deng, Y., Chen, J. W., Yang, S. & Dai, Y. J. An energetics tale of the 2022 mega-heatwave over central-eastern China. *npj Clim. Atmos. Sci.* **6**, 162 (2023).
- Ding, T., Gao, H. & Xie, T. J. Extreme warm spells may facilitate the new temperature record in 2023. *Environ. Res. Lett.* **19**, 041001 (2024).
- Ding, T., Yuan, Y., Zhang, J. M. & Gao, H. 2018: the hottest summer in China and possible causes. *J. Meteorol. Res.* **33**, 577–592 (2019).
- Perkins-Kirkpatrick, S. E. & Lewis, S. C. Increasing trends in regional heatwaves. *Nat. Commun.* **11**, 3357 (2020).
- Ren, L. W., Zhou, T. J. & Zhang, W. X. Attribution of the record-breaking heat event over Northeast Asia in summer 2018: the role of circulation. *Environ. Res. Lett.* **15**, 054018 (2020).
- Ye, Y. B. & Qian, C. Conditional attribution of climate change and atmospheric circulation contributing to the record-breaking precipitation and temperature event of summer 2020 in southern China. *Environ. Res. Lett.* **16**, 044058 (2021).
- Zhang, H. L. et al. Challenges and adaptations of farming to climate change in the North China Plain. *Clim. Change* **129**, 213–224 (2015).
- Wu, T. X., Li, B. F., Lian, L. S., Zhu, Y. B. & Chen, Y. F. Assessment of the combined risk of drought and high-temperature heat wave events in the North China plain during summer. *Remote Sens.* **14**, 4588 (2022).
- Lobell, D. B. & Field, C. B. Global scale climate–crop yield relationships and the impacts of recent warming. *Environ. Res. Lett.* **2**, 014002 (2007).
- Thornton, P. K., van de Steeg, J., Notenbaert, A. & Herrero, M. The impacts of climate change on livestock and livestock systems in developing countries: a review of what we know and what we need to know. *Agric. Syst.* **101**, 113–127 (2009).

29. McMichael, A. J. & Lindgren, E. Climate change: present and future risks to health, and necessary responses. *J. Intern. Med.* **270**, 401–4413 (2011).
30. Ridder, N. N., Ukkola, A. M., Pitman, A. J. & Perkins-Kirkpatrick, S. E. Increased occurrence of high impact compound events under climate change. *npj Clim. Atmos. Sci.* **5**, 3 (2022).
31. Li, B. H. et al. Future global population exposure to record-breaking climate extremes. *Earth's Future* **11**, e2023EF003786 (2023).
32. King, A. D. & Harrington, L. J. The inequality of climate change from 1.5 °C to 2 °C of global warming. *Geophys. Res. Lett.* **45**, 5030–55033 (2018).
33. Gong, D. Y., Pan, Y. Z. & Wang, J. A. Changes in extreme daily mean temperatures in summer in eastern China during 1955–2000. *Theor. Appl. Climatol.* **77**, 25–37 (2004).
34. Chen, R. D. & Lu, R. Y. Comparisons of the circulation anomalies associated with extreme heat in different regions of eastern China. *J. Clim.* **28**, 5830–5844 (2015).
35. Ding, T. & Ke, Z. J. Characteristics and changes of regional wet and dry heat wave events in China during 1960–2013. *Theor. Appl. Climatol.* **122**, 651–665 (2015).
36. Lu, R. Y. & Chen, R. D. A review of recent studies on extreme heat in China. *Atmos. Ocean Sci. Lett.* **9**, 114–1121 (2016).
37. Wang, H., Li, J. P., Zheng, F. & Li, F. The synergistic effect of the summer NAO and northwest Pacific SST on extreme heat events in the central–eastern China. *Clim. Dyn.* **61**, 4283–4300 (2023).
38. Chen, M. et al. Analyses on the heat wave events in Shanghai in recent 138 years. *Plateau Meteorol.* **32**, 597–607 (2013).
39. Cowan, T. et al. Factors contributing to record-breaking heat waves over the Great Plains during the 1930s Dust Bowl. *J. Clim.* **30**, 2437–2461 (2017).
40. Kysely, J. Temporal fluctuations in heat waves at Prague–Klementinum, the Czech Republic, from 1901–97, and their relationships to atmospheric circulation. *Int. J. Climatol.* **22**, 33–50 (2002).
41. Shevchenko, O., Lee, H., Snizhko, S. & Mayer, H. Long-term analysis of heat waves in Ukraine. *Int. J. Climatol.* **34**, 1642–1650 (2014).
42. Xie, T. J. et al. NAO implicated as a predictor of the surface air temperature multidecadal variability over East Asia. *Clim. Dyn.* **53**, 895–905 (2019).
43. Robson, J., Sutton, R., Menary, M. B. & Lai, M. W. K. Contrasting internally and externally generated Atlantic Multidecadal Variability and the role for AMOC in CMIP6 historical simulations. *Philos. T. R. Soc. A* **381**, 20220194 (2023).
44. Senapati, B., O'Reilly, C. H. & Robson, J. Pivotal role of mixed-layer depth in tropical Atlantic multidecadal variability. *Geophys. Res. Lett.* **51**, e2024GL110057 (2024).
45. Li, J. P. et al. Influence of the NAO on wintertime surface air temperature over East Asia: multidecadal variability and decadal prediction. *Adv. Atmos. Sci.* **39**, 625–642 (2022).
46. Li, J. P., Zheng, F., Sun, C., Feng, J. & Wang, J. Pathways of influence of the northern hemisphere mid–high latitudes on East Asian climate: a review. *Adv. Atmos. Sci.* **36**, 902–921 (2019).
47. Hirschi, M. et al. Observational evidence for soil-moisture impact on hot extremes in southeastern Europe. *Nat. Geosci.* **4**, 17–21 (2011).
48. Stéfanon, M., Drobinski, P., D'Andrea, F., Lebeaupin-Brossier, C. & Bastin, S. Soil moisture–temperature feedbacks at meso-scale during summer heat waves over Western Europe. *Clim. Dyn.* **42**, 1309–1324 (2014).
49. Deng, K. Q., Yang, S., Ting, M. F., Zhao, P. & Wang, Z. Y. Dominant modes of China summer heat waves driven by global sea surface temperature and atmospheric internal variability. *J. Clim.* **32**, 3761–3775 (2019).
50. Horton, R. M., Mankin, J. S., Lesk, C., Coffel, E. & Raymond, C. A review of recent advances in research on extreme heat events. *Curr. Clim. Change Rep.* **2**, 242–259 (2016).
51. Bartusek, S., Kornhuber, K. & Ting, M. North American heatwave amplified by climate change-driven nonlinear interactions. *Nat. Clim. Change* **12**, 1143–1150 (2022).
52. Choi, J. W., Song, C. Y., Kim, E. S. & Ahn, J. B. Possible relationship between heatwaves in Korea and the summer blocking frequency in the Sea of Okhotsk. *Int. J. Climatol.* **42**, 7497–7515 (2022).
53. Zhang, X. et al. Increased impact of heat domes on 2021-like heat extremes in North America under global warming. *Nat. Commun.* **14**, 1690 (2023).
54. Sun, C., Li, J. P., Ding, R. Q. & Jin, Z. Cold season Africa–Asia multidecadal teleconnection pattern and its relation to the Atlantic multidecadal variability. *Clim. Dyn.* **48**, 11–12 (2017).
55. Li, J. P. & Ruan, C. Q. The North Atlantic–Eurasian teleconnection in summer and its effects on Eurasian climates. *Environ. Res. Lett.* **13**, 024007 (2018).
56. Della-Marta, P. M. et al. Summer heat waves over western Europe 1880–2003, their relationship to large-scale forcings and predictability. *Clim. Dyn.* **29**, 251–271 (2007).
57. Rohde, R. A. & Hausfather, Z. The Berkeley Earth Land/Ocean temperature record. *Earth Syst. Sci. Data* **12**, 3469–3479 (2020).
58. Rayner, N. A. et al. Global analyses of sea surface temperature, sea ice, and night marine air temperature since the late nineteenth century. *J. Geophys. Res.* **108**, 4407 (2003).
59. Slivinski, L. C. et al. Towards a more reliable historical reanalysis: improvements for version 3 of the twentieth century reanalysis system. *Quart. J. Roy. Meteor. Soc.* **145**, 2876–2908 (2019).
60. Tang, X. X., Li, J. P., Zhang, Y. Z., Li, Y. J. & Zhao, S. Synergistic effect of El Niño and negative phase of NAO on winter precipitation in the southeastern United States. *J. Clim.* **36**, 1767–1791 (2023).
61. Watanabe, M. & Kimoto, M. Atmosphere–ocean thermal coupling in the North Atlantic: a positive feedback. *Q. J. R. Meteorol. Soc.* **126**, 3343–3369 (2000).

Acknowledgements

This work was jointly supported by the National Natural Science Foundation of China (42305032, 42175078, and 42175048), the Joint Research Project for Meteorological Capacity Improvement (22NLTSQ002), the Special Program for Innovation and Development of China Meteorological Administration (CXFZ2022J030), Anhui Meteorological Bureau Special Programme for Innovation and Development (CXB202301) and the Young Elite Scientists Sponsorship Program by BAST (BYESS2023205). We thank all the data and code providers, and the reviewers.

Author contributions

T.X., H.G. and T.D. contributed to the design of this study. T.X. prepared all figures and wrote the first draft of the manuscript. Data collection, consolidation, and analysis were performed by T.X., H.G., X.C. and W.W. All authors reviewed previous versions of the manuscript and approved the completed manuscript.

Competing interests

The authors declare no competing interests.

Additional information

Correspondence and requests for materials should be addressed to Hui Gao or Ting Ding.

Reprints and permissions information is available at <http://www.nature.com/reprints>

Publisher's note Springer Nature remains neutral with regard to jurisdictional claims in published maps and institutional affiliations.

Open Access This article is licensed under a Creative Commons Attribution-NonCommercial-NoDerivatives 4.0 International License, which permits any non-commercial use, sharing, distribution and reproduction in any medium or format, as long as you give appropriate credit to the original author(s) and the source, provide a link to the Creative Commons licence, and indicate if you modified the licensed material. You do not have permission under this licence to share adapted material derived from this article or parts of it. The images or other third party material in this article are included in the article's Creative Commons licence, unless indicated otherwise in a credit line to the material. If material is not included in the article's Creative Commons licence and your intended use is not permitted by statutory regulation or exceeds the permitted use, you will need to obtain permission directly from the copyright holder. To view a copy of this licence, visit <http://creativecommons.org/licenses/by-nc-nd/4.0/>.

© The Author(s) 2025